

## RESEARCH ARTICLE

10.1002/2014JB011014

## Key Points:

- Fault normal stiffness can be a proxy for contact area
- Postseismic changes in fault properties may be detectable
- Contact area and elastic properties can be measured simultaneously

## Correspondence to:

N. Beeler,  
nbeeler@usgs.gov

## Citation:

Nagata, K., B. Kilgore, N. Beeler, and M. Nakatani (2014), High-frequency imaging of elastic contrast and contact area with implications for naturally observed changes in fault properties, *J. Geophys. Res. Solid Earth*, 119, doi:10.1002/2014JB011014.

Received 1 FEB 2014

Accepted 30 MAY 2014

Accepted article online 3 JUN 2014

## High-frequency imaging of elastic contrast and contact area with implications for naturally observed changes in fault properties

Kohei Nagata<sup>1,2</sup>, Brian Kilgore<sup>3</sup>, Nick Beeler<sup>4</sup>, and Masao Nakatani<sup>1</sup>

<sup>1</sup>Earthquake Research Institute of the University of Tokyo, Tokyo, Japan, <sup>2</sup>Now at Ministry of Education, Culture, Sports, Science and Technology, Tokyo, Japan, <sup>3</sup>U.S. Geological Survey Earthquake Science Center, Menlo Park, California, USA, <sup>4</sup>U.S. Geological Survey Cascades Observatory, Vancouver, Washington, USA

**Abstract** During localized slip of a laboratory fault we simultaneously measure the contact area and the dynamic fault normal elastic stiffness. One objective is to determine conditions where stiffness may be used to infer changes in area of contact during sliding on nontransparent fault surfaces. Slip speeds between 0.01 and 10  $\mu\text{m/s}$  and normal stresses between 1 and 2.5 MPa were imposed during velocity step, normal stress step, and slide-hold-slide tests. Stiffness and contact area have a linear interdependence during rate stepping tests and during the hold portion of slide-hold-slide tests. So long as linearity holds, measured fault stiffness can be used on nontransparent materials to infer changes in contact area. However, there are conditions where relations between contact area and stiffness are nonlinear and nonunique. A second objective is to make comparisons between the laboratory- and field-measured changes in fault properties. Time-dependent changes in fault zone normal stiffness made in stress relaxation tests imply postseismic wave speed changes on the order of 0.3% to 0.8% per year in the two or more years following an earthquake; these are smaller than postseismic increases seen within natural damage zones. Based on scaling of the experimental observations, natural postseismic fault normal contraction could be accommodated within a few decimeter wide fault core. Changes in the stiffness of laboratory shear zones exceed 10% per decade and might be detectable in the field postseismically.

### 1. Introduction

The tectonic stresses that lead to earthquake slip are concentrated in regions of solid contact between asperities and gouge particles within a dilatant fault zone. Accordingly, many fault properties of interest to earthquake hazard research, e.g., occurrence time, recurrence interval, precursory slip, shear-induced dilatancy, time-dependent strength recovery, and triggered earthquake slip, are believed to be controlled by processes acting within the highly stressed contact regions. Unfortunately, contact-scale physical processes cannot be easily observed or measured directly for natural faults, and they are also difficult to observe even in controlled laboratory experiments.

For natural seismic fault zones, active seismic source studies show increases in wave speed following large earthquakes that continue for many years postseismically [e.g., *Li et al.*, 1998; *Li and Vidale*, 2001]. The increases that apparently occur within a broad, hundreds of meters wide “damage” zone are evident as fault zone trapped waves and decreases in trapped, *P* and *S* wave arrival times. Increases in wave speed over the decade following the 1992 Landers and 2004 Parkfield earthquakes are around 0.5 to 1% per year with the rate decreasing with time [*Li et al.*, 1998, 2006]. The wave speed changes are attributed to “strengthening” or “healing” of the fault zone following the earthquake via the progressive closure of coseismically generated cracks within the damage zone, presumed to be created as the earthquake rupture front propagates by. However, while there is a reasonable expectation that a reduction in crack density makes a fault zone stronger, the damage zone is a zone of sympathetic and secondary deformation induced by slip within the narrower fault core. The fault core is the locus of fault slip and is, by macroscopic or mechanical definition, the fault surface [*Chester and Chester*, 1998]. Accordingly, it is more likely that changes in physical properties of the fault core rather than the damage zone are relevant to understanding fault “strength” and earthquake mechanics.

Laboratory experiments of faulting have the advantage over active seismic source studies in that strength and mechanical properties are measured directly. Nonetheless, inferences about contact-scale processes

are also indirect, relying on the macroscopic mechanical data, for example, shear resistance in response to changes in slip speed [Dieterich, 1978, 1979], changes in normal stress [Linker and Dieterich, 1992; Kilgore et al., 2012], and time of static contact [Dieterich, 1972; Nakatani and Mochizuki, 1996], along with empirical or micromechanical models that relate an assumed contact-scale rheology to the macroscopic observations. Two notable exceptions are active source fault imaging techniques: transmitted light that measures real area of contact during frictional sliding [Dieterich and Kilgore, 1994, 1996] but only works with transparent samples and high-frequency elastic waves [Pyrak-Nolte et al., 1987, 1990; Yoshioka and Iwasa, 2006; Nagata et al., 2006, 2008] which work on any material but measures elastic contrast across the fault rather than contact area directly.

In the present study, to better understand relationships among the mechanical properties of faults, contact-scale deformation, and how those may be reflected by fault zone elastic properties, we simultaneously implement these two independent direct measurement techniques on a transparent fault. Based on our findings and following previous work [Nagata et al., 2008], we determine some conditions where active source imaging can be used on nontransparent samples so that this method can be used routinely to infer changes in contact area of actively slipping faults.

Theories of plastic and elastic friction provide necessary context on why the real area of contact is important in determining fault strength during frictional sliding and thus is background for understanding potential uses of transmitted light and seismic imaging techniques in fault mechanics research. The classic theory of friction [Bowden and Tabor, 1950] assumes contact-scale plastic yielding; to first order the average normal stress at an asperity contact  $\sigma_c$  is limited by the material yield strength, usually equated with the indentation hardness [e.g., Dieterich and Kilgore, 1996]. Shear load applied to the surface causes shear displacement at the average asperity contact shear strength,  $\tau_c$ , and shear strength is also a material constant due to yielding. Accordingly, friction  $f$ , the ratio of macroscopic shear stress  $\tau$  to effective normal stress  $\sigma_e$ , is equivalently the ratio of the contact-scale stresses,

$$f = \frac{\tau}{\sigma_e} = \frac{\tau_c}{\sigma_c}, \quad (1a)$$

and is approximately independent of normal stress. On the asperity scale, since contacts are always at the yield stress, independent of the applied normal force, the real area of contact  $A_c$  increases in proportion to the applied normal force,

$$A_c = A_T \frac{\sigma_e}{\sigma_c}, \quad (1b)$$

where  $A_T$  is the total fault surface area.

A result identical to equations (1a) and (1b) is found for man-made and some natural rough surfaces in purely elastic contact. For rough surfaces, increasing normal stress produces larger area at individual contacts and an increasing number of very small contacts as the rough surfaces are brought closer together. An increase in the number of contacts tends to reduce the average contacting area somewhat. The distribution of asperity heights is such that increments of increased normal stress bring the appropriate number of new asperities into contact to maintain constant average contact stress [Greenwood and Williamson, 1966; Walsh and Grosenbaugh, 1979; Brown and Scholz, 1985]. In particular, using a purely elastic model Greenwood and Williamson [1966] showed that for surfaces with roughness of laboratory test surfaces, with asperities assumed elastic, the total area of asperity contact increases essentially linearly over 4 orders of magnitude of increasing load. Though they assume a nonlinear elastic contact compliance, the resulting normal stress dependence of shear strength is the proportionality, (1a), and is entirely independent of the assumed contact-scale elastic interaction. In other words for this particular elastic model, the normal stress dependence of contact area (1b) is determined by the statistics of the surface topography. The contact normal stress  $\sigma_c$  is constant but not a material constant, the friction coefficient  $f$  is constant, and real area of contact is proportional to the applied normal load (1b).

Friction of bare rock surface appears to have both elastic [e.g., Scholz, 1988] and inelastic [Dieterich, 1972] components [Linker and Dieterich, 1992; Beeler, 2007; Kilgore et al., 2012]. The elastic and inelastic components are particularly obvious when normal stress is changed [Linker and Dieterich, 1992; Richardson and Marone, 1999;

*Hong and Marone, 2005; Kilgore et al., 2012*]: there are reversible elastic changes in contact area and fault normal displacement and subsequent slip-dependent inelastic changes in contact area and normal displacement. Light or elastic wave propagation imaging techniques allow for quantification of elastic and inelastic deformation during frictional sliding. Normal stress changes in experiments on Lucite plastic conducted for the present study illustrate these well, as will become clear later in this report. In fact, the preliminary results of the present study [*Nagata et al., 2010*] were the primary motivation for the *Kilgore et al. [2012]* work on granite.

### 1.1. Transmitted Light Intensity

For rock friction the dependence of real area of contact on applied normal stress, equation (1b) was first demonstrated using light transmitted across sliding surfaces between transparent minerals, silica glass, and analogue materials [*Dieterich and Kilgore, 1994, 1996*]. When the fault surfaces are brought together, contact is established at small regions where light is easily transmitted through the surface. Elsewhere, the light striking the roughened surfaces is scattered. Thus, when corrected for scattering, the total amount of transmitted light is proportional to the real area of asperity contact. To quantify the transmitted light, a photodiode attached to a microscope is focused on the sliding surface; the output voltage measures the intensity of the light transmitted across the sliding surfaces light intensity ( $I$ ) and provides a continuous record of total contact area. Photodiode output can be converted to fractional contact area,  $A$ , (e.g., contact area/area of sliding surface) using reference measurements of the average light intensity at points of contact and for regions not in contact,

$$A = \frac{A_c}{A_T} = \frac{I - I_0}{I_{100} - I_0}, \quad (2)$$

where  $I$  is the photodiode output (volts) measured during an experiment. The calibration reference values  $I_0$  and  $I_{100}$  are the measured reference photodiode outputs for equivalent contact areas of 0 and 100%, respectively. The chief limitation to using this LI technique to study faulting is that it requires transparent samples. Additional limitations are associated with the wavelength of light. Contacts that are smaller than the light wavelength and subwavelength sized voids within contacts may not be detected.

### 1.2. Transmitted Acoustic Wave Amplitude

Recently scientists at the Earthquake Research Institute, University of Tokyo (ERI) [*Nagata et al., 2008*] have applied an active seismic imaging technique to slipping fault zones that does not require transparency [*Kendall and Tabor, 1971; Pyrak-Nolte et al., 1990; Yoshioka and Iwasa, 2006*]. The approach is to send low-amplitude, high-frequency elastic waves across the fault, propagating normal to the fault plane. A function generator outputs a single period, small amplitude sine wave voltage to a piezoelectric transducer. The acoustic wave generated by the transducer crosses the fault and is recorded by a high-speed digitizer on the opposite side. The signal is sent rapidly enough to produce an effectively continuously sampled record of the transmitted amplitude. The wavelength is large,  $\sim 2.5$  mm, relative to the asperity contacts which are microns to a few tens of microns in radius. Since the acoustic waves are traveling elastic distortions, their transmitted amplitude is sensitive to the elastic properties. The fault is an interface of elastic contrast relative to the surrounding material, having reflection and transmission coefficients commensurate with the magnitude of the contrast [*Kendall and Tabor, 1971; Schoenberg, 1980; Pyrak-Nolte et al., 1987, 1990*]. By treating the fault as a displacement discontinuity, wave propagation theory relates the relative amplitude  $T$  of the transmitted wave, the transmission coefficient, to interface stiffness  $k$  as

$$T = \frac{a_t}{a_0} = \left[ 1 + \left( \frac{k_*}{k} \right)^2 \right]^{-\frac{1}{2}}, \quad (3)$$

[*Kendall and Tabor, 1971; Schoenberg, 1980; Pyrak-Nolte et al., 1987*]. Here  $a_t$  is the transmitted amplitude (in volts),  $a_0$  is the amplitude of the incident wave, equivalently the transmitted amplitude in the absence of an interface (no elastic contrast at the fault plane),  $k$  is the specific interface elastic stiffness,  $k_*$  is a constant  $k_* = \omega \rho v / 2$  where  $\omega$  is angular frequency of the wave ( $2\pi \times 10^6$ /s in our experiments),  $\rho$  is density ( $1.19 \text{ g/cm}^3$ ), and  $v$  is the elastic wave propagation speed ( $2573.9 \text{ m/s}$  at this frequency). For our experiments in Lucite plastic  $k_*$  is  $9.62 \text{ MPa}/\mu\text{m}$ . While at high frequencies  $k_*/k \gg 1$   $T$  is proportional to

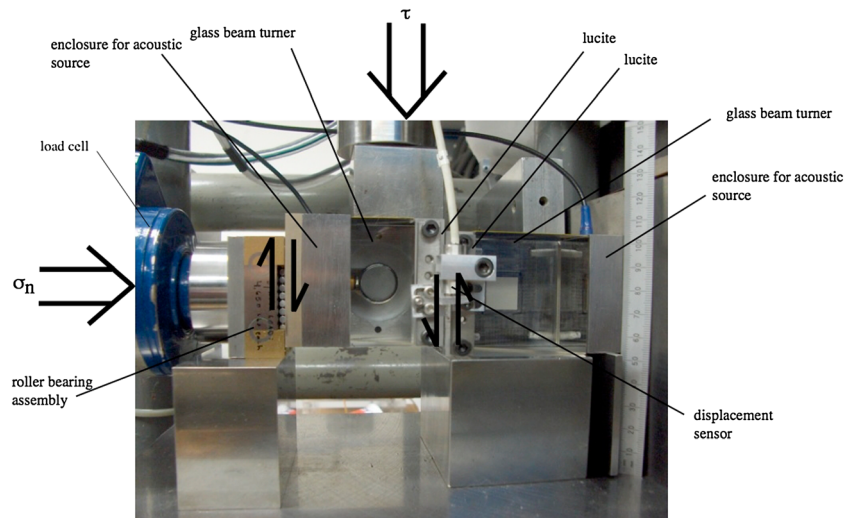


**Figure 1.** Annotated photograph of the geometry and loading of the experimental fault. The configuration from left to right is load cell for measuring normal stress, roller bearing, steel enclosure for acoustic receiver, optical beam turner (glass), moving sample (Lucite), stationary sample (Lucite), steel enclosure for acoustic source, steel spacer blocks. The fault displacement sensor in front has a white wire protruding from it. At the top, the loading platen for shear stress is partially visible. On right is a metric ruler for scale; each tick on the left side of the ruler closest to the samples = 1 mm.

the stiffness [Yoshioka and Iwasa, 2006], we use the complete relation (3) throughout this study. For shorthand we will refer to measurements of the transmitted amplitude as AT.

### 1.3. Purpose

Our study is to make detailed measurements of the frictional properties of a transparent laboratory fault while simultaneously employing both the LI and AT techniques (Figure 1). The principal objective is to establish the relationship between contact area and elastic fault stiffness. We show that at steady state conditions the known fractional contact area can be empirically related to the specific fault zone stiffness measured by the transmitted waves. Then transmitted amplitude measurements can be used to infer changes in contact area in subsequent experiments on nontransparent materials. Knowing something about the relationship of elastic properties to real area of contact, a secondary objective is to relate results from laboratory-scale fault zone imaging to comparable measurements of the changes in elastic properties made in active seismic source and geodetic studies of natural fault zones. We show that changes in fault stiffness observed using 1 MHz seismic waves in the laboratory imply wave speed changes that are smaller by about a factor of 2 than those observed in postseismic imaging studies made in the 100 Hz frequency range such as following the Landers earthquake. However, the changes in fault zone stiffness may be much larger and detectable in a natural setting using transmitted amplitude.

The organization of the following report differs somewhat from the standard experiments, results, discussion/analysis structure of most laboratory papers. We first describe the experimental and measurement techniques (section 2) as is normally done. Then we focus on the results from steady state conditions over the range of slip speeds and normal stresses where we establish empirical relations between contact area and fault stiffness (section 3). Immediately following those results is a section where the steady state results are analyzed, related to previous studies of rock friction and the physical interpretation and implications are discussed (section 4). These are the principal experimental findings of this study. Included in the analysis of the step test results, we briefly touch on whether the transmitted amplitude can be easily related to contact area for nontransparent samples or at nonsteady state conditions. There, we describe results from single order of magnitude rate steps and the hold portion of slide-hold-slide test where the same relations seen at steady state seem to stand up. Generally, we find that the relationship between contact area and fault stiffness far from steady state is more complicated and that remains a topic for a subsequent paper. In the final section of the paper (section 5) we apply the results from measurements of contact area, fault normal

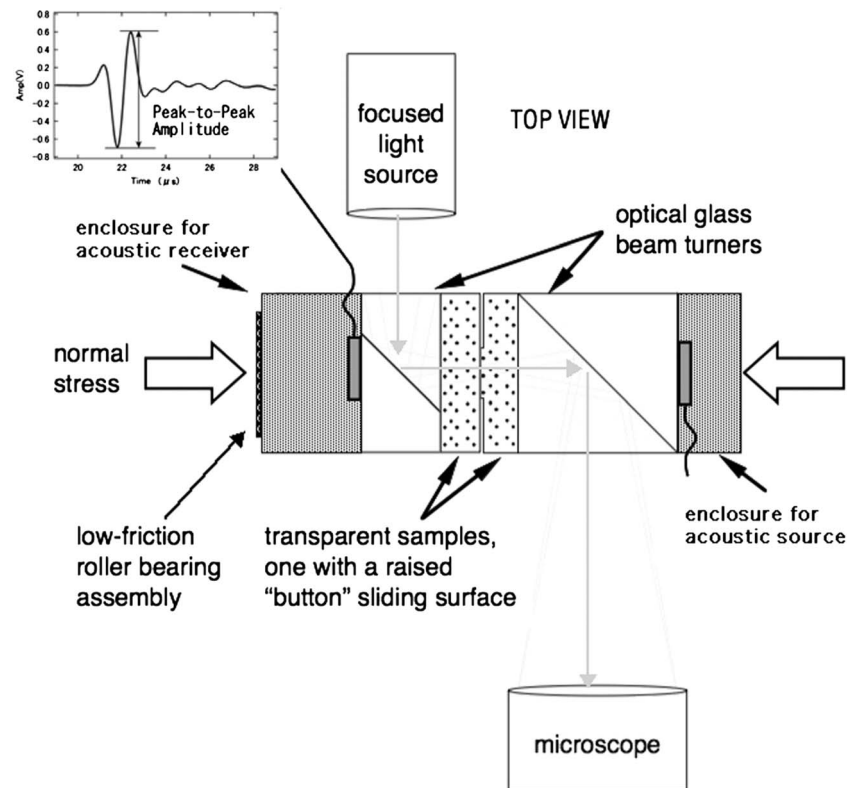


**Figure 2.** Annotated sketch of the system used to image contact area and measure transmitted wave amplitude. Light from the source reflects off the left glass beam turner, travels across the fault surface, and is reflected off the right beam turner into the microscope where light intensity is measured by a photodiode. Acoustic waves are emitted from the source on right, transmitted across the fault and recorded at the receiver on left. Slip on the fault is left lateral, see Figure 1.

displacement, and fault normal stiffness made during hold tests to the analogous natural observations of changes in elastic properties and strain made postseismically.

## 2. Experiments

A double direct shear apparatus [Dieterich, 1978] was adapted for use in these experiments following Dieterich and Kilgore [1994] and Nagata *et al.* [2008]. The apparatus permits servo control of sliding speeds from  $10^{-4}$   $\mu\text{m/s}$  to  $10^3$   $\mu\text{m/s}$  at normal stresses to 150 MPa. For the transmitted light measurements the apparatus is modified by replacing one of the faults with a roller bearing assembly and using 45° optical grade glass beam turners through which light illuminates the fault surface normal to the sliding direction while supporting the normal stress applied to the samples (see Figures 1 and 2). Stress on the beam turners is reduced to 10% of the stress on the sliding surface by grinding away 90% of the original 50.0 mm  $\times$  50.0 mm roughened sliding surface leaving a small raised square button approximately 15.8 mm  $\times$  15.8 mm on each side and 1 mm high on the sample face. The transmitted light observation system employs a long working distance microscope fitted with a photovoltaic silicon photodiode. The illuminating light source utilizes a focusing system matched to the microscope optics to minimize point diffraction and has a narrow bandwidth (10 nm) interference filter (550 nm center wavelength) to eliminate chromatic aberration. Intensity is also measured at the source so that the transmitted light can be corrected for variation of the source.

The AT methodology as developed for active seismic monitoring during frictional sliding at ERI Tokyo was implemented jointly at the U.S. Geological Survey (USGS) by Kohei Nagata (ERI) and Brian Kilgore (USGS). In the experiments (Figure 1), we measured the amplitude of a fault normal incident pulse transmitted across the fault as well as across interfaces between the various components of the LI system. The experiments use a broadband *P* wave transducer with a central frequency of 1 MHz (Panametrics V103RM). The transducer element is 1.3 cm across. This is the same type of transducer used in previous laboratory friction studies

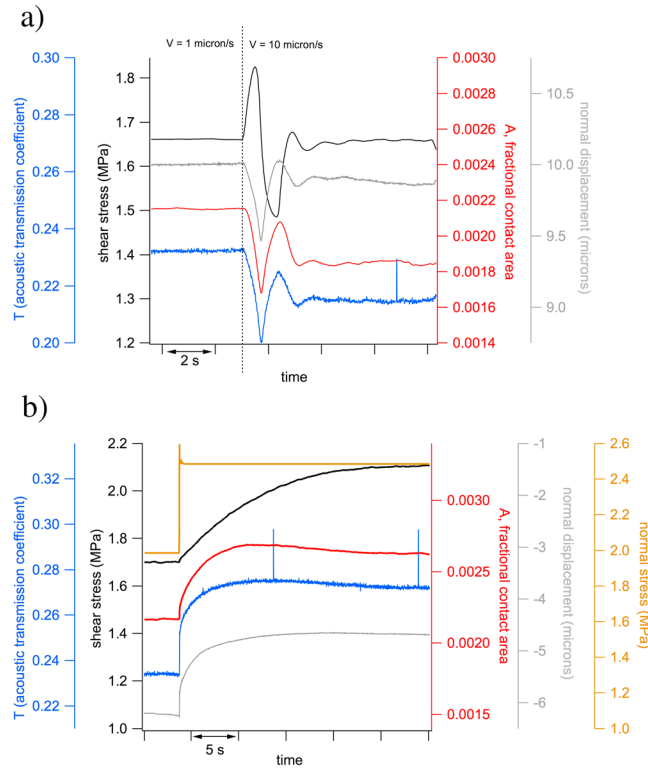


**Figure 3.** Detailed response to changes in (a) sliding speed and (b) normal stress. (a) A loading velocity step increase from 1 to 10  $\mu\text{m/s}$ , imposed at the vertical dashed line. Vertical axes show shear stress (black),  $T$  (blue),  $A$  (red), and fault normal displacement (grey). The spikes in  $T$  are likely processing errors in determining transmitted amplitude. Positive changes in normal displacement indicate compaction.  $T$  and contact area show nearly identical responses. Normal displacement shows an essentially identical response—these normal displacement data have been corrected for an approximately linear displacement trend that results either from surface wear or from slight misalignment of the sensor. (b) A normal stress step increase from 2 to 2.5 MPa. Vertical axes are the same as in Figure 3a except that normal stress (yellow) has been added. The response of  $T$  and contact area show similar but not identical responses, consisting of an instantaneous response followed by a transient of the same sense. The fault normal displacement has been corrected for elastic effects as described in Appendix A. Neither  $T$  or contact area are similar to the response of shear stress which has no instantaneous response and a much longer slip transient.

Similar acrylic has been used and in a number of subsequent laboratory faulting studies [McLaskey et al., 2012; Svetlizky and Fineberg, 2014]. The elastic modulus of Lucite is lower than for rock by around an order of magnitude (see section 5.3 below) and the steady state rate dependence is somewhat more negative (see section 3.3 below). Other than those differences that can easily be accounted for, the friction of bare surfaces of Lucite quite closely resemble that of granite or quartzite at room temperature and have similar relevance in application to the earth. The sliding surfaces were roughened by hand lapping with # 60 SiC abrasive. Normal stresses were between 1 MPa and 2.5 MPa at slip speeds from 0.01 to 10  $\mu\text{m/s}$ . Due to the low normal stresses, the fractional contact area is very small, ranging from around 0.001 up to about 0.003 while the fault normal stiffness calculated from equation (3) is between 1 and 3 MPa/ $\mu\text{m}$ . Tests consist of standard rate steps [Dieterich, 1979] (Figure 3a), slide-hold-slide tests [Dieterich, 1972], normal stress steps [Linker and Dieterich, 1992] (Figure 3b), low shear stress holds (near static) [Nakatani and Mochizuki, 1996], and normal stress steps at low shear stress (near static). In this report we focus on the results from steady state conditions at different slip rates and normal stresses and transient behavior in rate step tests and during hold tests.

[Nagata et al., 2008, 2012]. A sine wave is used as the source and the digital records of the received wave are made at 100 million samples/s. One source signal is sent every 10 milliseconds resulting in an effectively continuously sampled record of the transmitted amplitude. Transmitted amplitude was calculated as in equation (3), where  $a_0$  is the amplitude of the pulse that has passed through the same optical component interfaces and the same path length of intact Lucite. In the configuration of the present experiments, the relative position of the ultrasonic transmitter and receiver as measured parallel to the interface changes as the sliding proceeds. Though this is not ideal, motion of the sensor receiver pair does not produce detectable displacement-dependent changes in the transmitted amplitude. In addition to the LI and AT data, we record shear stress, normal stress, fault slip measured across the interface (Figure 1), and fault normal displacement. Normal stress is servo controlled using the output from the load cell. The fault slip measurement is used as the feedback signal for the separate servo system that produces shear displacement of the fault. Thus, fault slip is also a control variable, better described as the elastic load point displacement of the testing machine.

The experiments were conducted on transparent samples made from L cast acrylic sheet Lucite, made by Dupont. This is the same material used by Dieterich and Kilgore [1994, 1996].

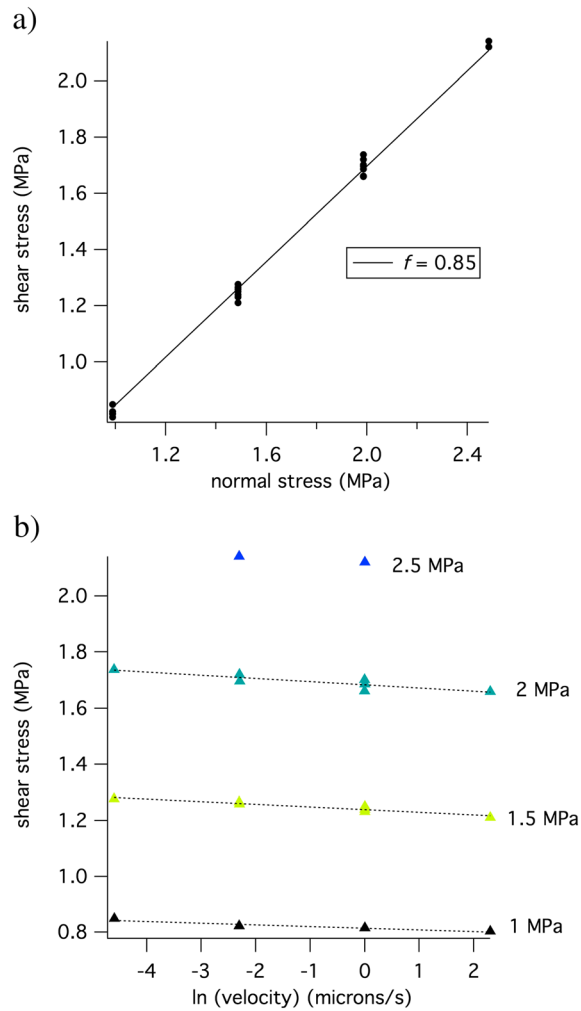


**Figure 4.** Dependence of shear stress on normal stress and sliding velocity. (a) Shear stress versus normal stress for four normal stresses between 1 and 2.5 MPa. Much of the spread in the data at each normal stress is due to these measurements being made at a range of sliding speeds between 0.01  $\mu\text{m/s}$  and 10  $\mu\text{m/s}$ . The shear resistance depends strongly on the normal stress. (b) Same data in Figure 4a plotted versus natural logarithm of the slip speed. There is a very weak dependence on the slip speed. Dashed lines are fits to the data at each normal stress. The symbol colors reflect the normal stress as labelled.

individual asperities in sliding contact [Scholz and Engelder, 1976], and sliding between bare rock surfaces [Dieterich and Kilgore, 1996]. The interpretation, attributable to Dieterich [1978, 1979], is that ongoing time-dependent creep of asperities under fault normal loading is modulated by the slip speed. This results in the surface separation being larger and contact area being smaller due to shorter contact lifetime the higher the sliding speed.

### 3.2. Normal Stress Step Tests

Associated with a change in normal stress (Figure 3b) are instantaneous changes in normal displacement (grey), contact area (red), and acoustic transmission (blue). Unlike the rate steps, for step increases in normal stress during sliding at constant slip speed, contact area and transmitted amplitude show a similar but not identical response. The contact area change indicates that indeed there are elastic changes in area but most of the change in contact area evolves over time or slip. Transmitted acoustic amplitude also shows an instantaneous response that is large relative to that of contact area, and that is followed by a similar-sized

### 3. Experimental Results

The initial condition in slip rate step and normal stress step experiments (Figure 3) is steady state. The change in the control variable results in transient changes in fault properties that evolve over time or displacement to new steady state values. As discussed in detail in the immediately following subsections, contact area and fault stiffness track each other closely during order of magnitude rate steps. The relationship is more complicated for normal stress steps.

#### 3.1. Rate Step Tests

Individual rate step tests indicate a rate-weakening response where shear strength decreases with sliding rate (Figure 3a). The fault is rate weakening over the entire range of tested speeds (0.01 to 10  $\mu\text{m/s}$ ) and normal stresses (see section 3.3 and Figure 4). The transient responses of fractional contact area, acoustic transmission coefficient and normal displacement to a change in sliding speed are nearly identical (compare red, blue, and gray traces in Figure 3a). Here and throughout, the absolute values of fault normal displacement are arbitrary while the relative changes are of interest. The sign convention for fault normal displacement is a positive change indicates compaction. The measurements in Figure 3a show net decreases in contact area and transmitted amplitude and a dilation associated with increases in slip speed. For the contact area and normal displacement data, the observations are consistent with previous studies of

**Table 1.** Steady State Values From Slip Rate and Normal Stress Step Tests<sup>a</sup>

Test Type	Sequence #	$\sigma_n$ (MPa)	$\tau$ (MPa)	$V$ ( $\mu\text{m/s}$ )	$A$	$T$	Normal Displacement ( $\mu\text{m}$ )	Estimated Areal Density ( $\mu\text{m}$ ) <sup>-2</sup>	Estimated Contact Spacing ( $\mu\text{m}$ )	$k$ (MPa/ $\mu\text{m}$ )
ns	20	2.5	2.1	1	0.00259	0.277	13.46	9.2e-05	104.5	2.77
ns	6	1.5	1.2	1	0.00166	0.189	4.48	5.9e-05	130.3	1.85
ns	13	2	1.7	1	0.00211	0.235	9.68	7.5e-05	115.8	2.32
rs	2	1	0.82	1	0.00112	0.139	-1.47	4.0e-05	158.7	1.36
rs	5	1	0.82	0.1	0.00135	0.159	-0.15	4.8e-05	144.8	1.55
rs	14	2	1.7	0.1	0.00258	0.262	10.60	9.1e-05	104.7	2.61
rs	4	1	0.82	1	0.00103	0.14	-1.02	3.6e-05	165.9	1.37
rs	8	1.5	1.3	0.01	0.00285	0.244	6.75	1.0e-04	99.6	2.42
rs	9	1.5	1.3	0.1	0.00215	0.214	5.89	7.6e-05	114.7	2.11
rs	10	1.5	1.2	1	0.00166	0.19	5.26	5.9e-05	130.4	1.86
rs	11	1.5	1.2	10	0.00133	0.173	5.04	4.7e-05	145.8	1.69
rs	12	1.5	1.3	1	0.00162	0.192	5.57	5.7e-05	132.3	1.89
rs	15	2	1.7	0.01	0.00341	0.294	11.44	1.2e-04	91.0	2.96
rs	7	1.5	1.3	0.1	0.0021	0.215	5.72	7.4e-05	116.1	2.12
rs	3	1	0.8	10	0.000914	0.125	-1.68	3.2e-05	175.9	1.22
rs	16	2	1.7	0.1	0.0026	0.258	10.49	9.2e-05	104.4	2.57
rs	17	2	1.7	1	0.00215	0.232	10.00	7.6e-05	114.6	2.30
rs	18	2	1.7	10	0.00185	0.215	9.87	6.6e-05	123.5	2.12
rs	19	2	1.7	1	0.00217	0.239	10.37	7.7e-05	114.2	2.37
rs	1	1	0.82	0.1	0.00163	0.158	-0.94	5.8e-05	131.7	1.54
rs	21	2.5	2.1	0.1	0.00307	0.306	14.22	1.1e-04	96.0	3.09
rs	0	1	0.85	0.01	0.00228	0.182	-0.01	8.1e-05	111.4	1.78

<sup>a</sup>(070710 experiment). Test types are normal stress step (ns) and rate step (rs).

transient. The transient has similar duration as the transient contact area change. The normal displacement data most closely resembles the transmitted amplitude; there is an instantaneous change followed by a similar-sized transient.

The change in shear resistance following a normal stress step is similar to observations for rock made recently by *Kilgore et al.* [2012] (Figure 3b). There is essentially no instantaneous change in shear stress (black) when the normal stress is changed (yellow). Shear stress follows slip-dependent evolution. Despite the contact area changing rapidly, there is no rapid change in shear resistance. Apparently, the instantaneously created contact area must be somehow loaded by slip on the interface or sheared an appreciable distance to contribute to the resistance. These Lucite observations [*Nagata et al.*, 2010] were the primary motivation for the *Kilgore et al.* [2012] study of the response rock friction to normal stress. For both Lucite and rock, the shear stress response is qualitatively similar to observations made during impact tests on metal surfaces [*Prakash*, 1998].

### 3.3. Steady State Conditions

To quantify the relations among shear stress, normal displacement, contact area, and transmitted amplitude, at a given slip speed and normal stress, the steady state values are measured to produce a single value of each variable for those conditions (Table 1). Shear resistance is proportional to normal stress with a friction coefficient of  $\sim 0.85$ , not unlike Byerlee's Law [*Byerlee*, 1978] (Figure 4a), and consistent with equation (1a). In addition shear strength depends weakly on slip rate (Figure 4b) with the strength decreasing with the natural logarithm of the sliding velocity much as it does at steady state for bare surfaces of quartzofeldspathic rock [*Dieterich*, 1979]. The implied rate dependence of strength is negative and increases with normal stress. The rate dependence normalized by normal stress,  $df/d \ln v = -0.006$ , is somewhat more negative than the steady state rate dependence for granite or quartzite (approximately  $-0.004$ ) [*Kilgore et al.*, 1993].

Both fractional contact area and  $T$  vary approximately linearly with normal stress; however, the intercepts are different at different sliding speeds (Figure 5), indicating that contact area and stiffness diverge somewhat when normal stress is changed as was depicted in Figure 3b. The sense of the dependence of contact area on sliding speed is as expected from previous observations on Lucite [*Dieterich and Kilgore*, 1994] and from friction theory: at lower sliding speed, the area of contact is larger due to more

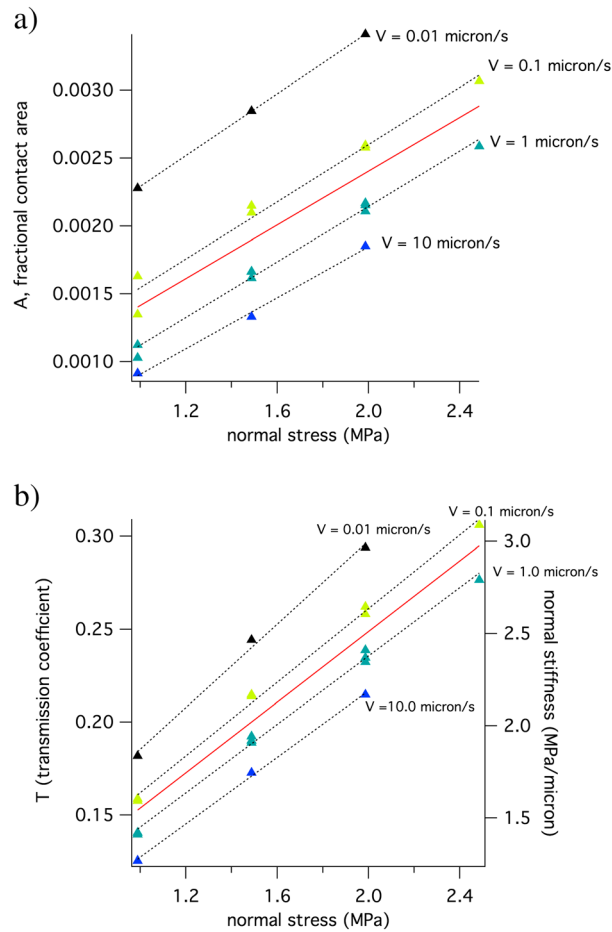


**Figure 5.** Average values of (a) contact area and (b) transmitted amplitude over a range of normal stresses and slip speeds. Superimposed dashed lines are fits to the data at each slip rate. The red lines are fits to the entire data set. In Figure 5b the right axis, fault normal stiffness is calculated from the measured  $T$  using equation (3).

to result from changes in the amount of yielding at asperity contacts as required by the different average contact lifetimes at each sliding speed.

#### 4. Analysis and Discussion

While we are primarily interested in understanding the relationship between real area of contact and transmitted amplitude in these experiments, to establish a qualitative physical basis for a calibrated relationship between those two quantities, in the following section, where possible, we develop conceptual models to explain the fundamental relations between contact area, normal displacement, and fault stiffness. The resulting relationships are shown to be consistent with the observations detailed in the present study and also to other previous rock friction studies. Generally, we find relations among contact area, transmitted amplitude, normal displacement, normal stress, and slip speed conform to expectations from existing models of frictional sliding on rough fault surfaces.

##### 4.1. Elastic Normal Displacement, Fault Normal Stiffness, and Contact Area

The net change in normal displacement from the combined elastic and inelastic responses depends logarithmically on the normal stress (Figure 6a). Since the acoustic transmission coefficient measures the dynamic normal elastic stiffness of the fault, that is, the derivative of normal stress with respect to elastic normal displacement, the physics underlying the elastic component of normal displacement is a key to understanding the fundamental mechanics of elastic wave propagation in faulted rock. Elastic models of rough rock surfaces in

contact-scale yielding (cf. equation (1b)) at the longer contact lifetimes. The transmitted amplitude also depends on sliding rate in the same manner as contact area, decreasing with increasing sliding velocity. The relation between stiffness and normal stress is also qualitatively as expected from contact mechanics: normal stiffness increases with normal stress [Johnson, 1985].

Normal displacement is nonlinear in normal stress and is reasonably well fit with a logarithmic dependence (Figure 6a). Similar to contact area, transmitted amplitude and shear resistance, normal displacement depends logarithmically on slip speed (Figure 6b). The dependence on slip speed is similar to observations of porosity made in friction experiments on gouge layers [Marone et al., 1990] and normal displacement of bare surfaces [Beeler and Tullis, 1997] of quartzofeldspathic rock at constant normal stress. Note that these normal displacement measurements shown in Figure 6b contain the instantaneous (elastic) and transient (inelastic) components apparent in the normal step test shown in Figure 3b. The inelastic response is probably well isolated in the tests at constant normal stress. That is, at a particular normal stress, the variation with sliding velocity is likely

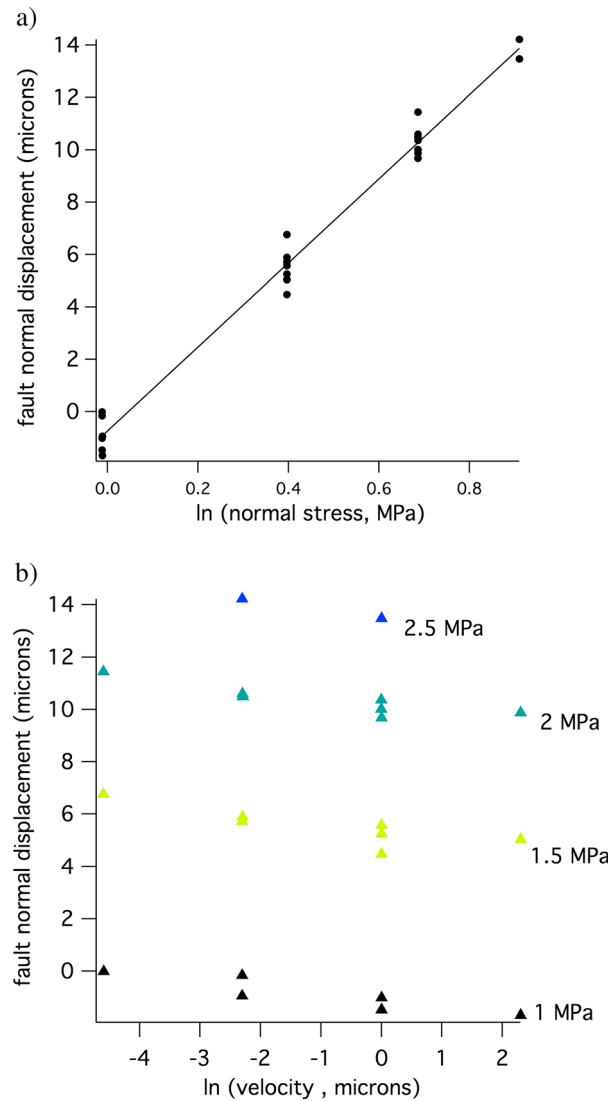


**Figure 6.** Dependence of normal displacement on normal stress and sliding velocity. (a) Normal displacement versus the natural logarithm of normal stress for four normal stresses between 1 and 2.5 MPa. Much of the spread in the data at each normal stress is due to these measurements being made at a range of sliding speeds between 0.01  $\mu\text{m/s}$  and 10  $\mu\text{m/s}$ . Normal displacement depends strongly and nonlinearly on the normal stress. The black line is a fit to the data with slope of 16  $\mu\text{m}$ . (b) Same data as in Figure 6a plotted versus natural logarithm of the slip speed. There is a weak dependence on the slip speed. The symbol colors reflect the normal stress as indicated by the label on the right.

asperity heights in contact at any given load can be well approximated by an exponential function  $\varphi(z) \propto \exp(-z/C)$ , and this has been shown to be an excellent approximation for many natural and laboratory rock surfaces [Walsh and Grosenbaugh, 1979; Swan, 1983; Power and Tullis, 1992]. Using this exponential height distribution, Beeler and Hickman [2001] showed that if the resisting force of an individual asperity has the general form  $F = C_1(z - d)^p$  where  $p$  is a positive exponent and  $C_1$  is a constant then the solution to (4b) is

$$\sigma_n = \eta C_2 \exp\left(\frac{-d}{C}\right). \quad (5a)$$

That is, the same relation between normal displacement and normal stress arises largely independent of the details of the elastic asperity compliance. For example, if the compliance is entirely in the region of contact

contact based on Greenwood and Williamson [1966], such as Brown and Scholz [1985] and Yoshioka [1994], suggest generally that normal displacement depends logarithmically on normal stress, as follows.

Greenwood and Williamson [1966] considered contact between a perfectly flat surface and another surface that is nominally flat but covered with fine-scale topography. Later, Brown and Scholz [1985] showed that the same formalism can be used to consider two nominally flat but rough surfaces in contact by constructing a composite surface profile that is the sum of the two rough profiles. In either case, when the surfaces are brought together to separation of  $d$ , the probability that any asperity on the rough surface will make contact is

$$P = \int_d^{\infty} \varphi(z) dz, \quad (4a)$$

where  $\varphi(z) dz$  is the probability that a particular asperity has height  $z$  in the range  $z + dz$ . Assuming that all asperity contacts deform elastically and that the force  $F$  exerted by a single asperity is a function of the local deformation  $z - d$  ( $F(z - d)$ ), the total macroscopic resisting normal stress  $\sigma_n$  is

$$\sigma_n = \eta \int_d^{\infty} F(z - d) \varphi(z) dz \quad (4b)$$

where  $\eta$  is the areal density of asperities ( $\text{area}^{-1}$ ) on the surface [Greenwood and Williamson, 1966]. To apply equation (4b) requires specifying the function  $\varphi$  for distribution of asperity heights on the surface and the function  $F$  that characterizes the contact normal forces.

Greenwood and Williamson [1966] suggested that the distribution of

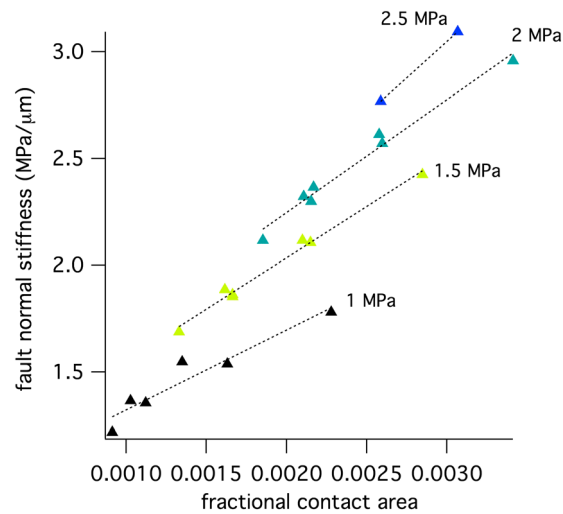


**Figure 7.** The relationship between dynamic fault normal stiffness and fractional contact area over the entire range of normal stresses and slip speeds. These are the same data shown in Figures 5a and 5b. In this figure the color coding differs from those figures and indicates normal stress. Superimposed curves are linear fits to the data at each normal stress.

stress is increased the separation between the surfaces decreases resulting in increased strain at each contact. In addition, other asperities come into contact as the separation decreases. The resistance to normal displacement arises primarily due to the number of asperities in contact, controlled by the statistics of the asperity population, rather than the details of the elastic behavior of the asperities themselves.

The expected fault normal compliance of rough laboratory fault surfaces results from taking the derivative of (5b) with respect to normal stress; the stiffness is the reciprocal

$$k_n = \frac{d\sigma_n}{d\delta} \propto \sigma_n. \tag{5c}$$

The prediction is consistent with the observed relation for the specific stiffness (Figure 4b) from the transmitted amplitude measurements.

Real area of contact is linear in normal stress (Figure 5) consistent with standard elastic and plastic theories of friction, equation (1b), and the linear relation between shear and normal stress (Figure 5a) expected from those same theories, equation (1a).

#### 4.2. Relation of Specific Normal Stiffness to Fractional Contact Area

As both stiffness and fractional contact area are approximately linearly related to normal stress at a single slip rate (Figure 5) but show different zero intercepts at each rate, the relationship between stiffness and contact area is nonunique (Figure 7). Fortunately, these two measurements vary systematically in a way that can be characterized empirically and perhaps ultimately reconciled with models of a multicontact interface. For the time being, we use our measured values of both variables to produce a calibration that converts measured stiffness to contact area at any normal stress and slip rate for these transparent samples.

##### 4.2.1. Calibration for Transparent Samples

*Kendall and Tabor* [1971] showed that so long as the total surface area exceeds the real area of contact by a factor of 10 or more, asperity contacts have little elastic interaction; in the limit of isolated individual contacts the interface, stiffness is the sum

$$k = Nk_c, \tag{6a}$$

where  $N$  is the number of contacts and  $k_c$  is the average single contact stiffness. Note that here and throughout stiffness is in units of stress per distance, whereas *Kendall and Tabor* [1971] used units of force/distance. If the contact area is large or the spacing of contacts is clustered the contacts interact and in the limit of adjacent contacts the interface stiffness goes as  $\sqrt{N}$ , instead of the proportionality (6a). Because contact area in our

(Hertzian contact,  $p = 3/2$ ) or increases in proportion to the amount of deformation ( $p = 1$ ), then the form (5a) holds. Noting that the surface separation  $d$  is related to measured normal displacement as  $d = d_0 - \delta$  where  $d_0$  is the height of the tallest asperity above the reference surface, normal displacement varies with normal stress logarithmically

$$\delta = \delta_0 + C \ln \frac{\sigma_n}{\eta C_2}. \tag{5b}$$

In addition to being consistent with our observed relation between normal displacement and normal stress (Figure 6a), equation (5b) is the empirical relationship commonly used to relate normal stress to elastic joint normal displacement [*Goodman*, 1976]. By way of a physical explanation of (5b), for rough surfaces in contact, as normal

**Table 2.** Fit Parameters From Calibration Development

Data Source	$\sigma_n$ (MPa)	Independent Variables	Dependent Variable	Equation	Parameters
Table 1	1	A	k	(7)	$k_0 = 0.95 \text{ MPa}/\mu\text{m}$ $\beta = 373 \text{ MPa}/\mu\text{m}$
Table 1	1.5	A	k	(7)	$k_0 = 1.0 \text{ MPa}/\mu\text{m}$ $\beta = 482 \text{ MPa}/\mu\text{m}$
Table 1	2	A	k	(7)	$k_0 = 1.2 \text{ MPa}/\mu\text{m}$ $\beta = 529 \text{ MPa}/\mu\text{m}$
Table 1	2.5	A	k	(7)	$k_0 = 1.0 \text{ MPa}/\mu\text{m}$ $\beta = 680 \text{ MPa}/\mu\text{m}$

experiments is many hundreds of times smaller than total area, (6a) is expected to be a good approximation of how the fault stiffness changes with number of contacts.

We can further characterize the nature of the contact population by estimating the areal density of contacts. Noting that total contact area for circular contacts is  $A_c = N\pi r^2$ , where  $r$  is the average contact radius, the areal density of asperities is  $\eta = N/A_T = A/\pi r^2$ . Following *Tullis et al.* [1993], *Beeler et al.* [2008] showed that for a population of sliding asperity contacts to first order the characteristic slip distance  $d_c \approx r$ . The slip distances inferred from our rate stepping tests (Figure 3) are short and using  $d_c = 3 \mu\text{m}$ , we estimate a mean areal density of  $\sim 7 \times 10^{-5}/\mu\text{m}^2$  (Table 1). The average contact spacing  $\Delta c = \sqrt{1/\eta}$  is  $\sim 120 \mu\text{m}$ . In addition, *Kendall and Tabor* [1971] showed in analysis of different contact geometries that the stiffness of an individual asperity  $k_c$  varies in proportion with the contact dimension, therefore as square root of the contact area. Thus, a *Kendall and Tabor* [1971] model predicts that interface stiffness should vary as the square root of the fractional contact area at fixed contact geometry and number of contacts

$$k \propto N(\sigma_n, V)\sqrt{A}, \tag{6b}$$

where the number of contacts depends on normal stress and slip speed. While the number of contacts will vary approximately exponentially with fault normal displacement [*Greenwood and Williamson, 1966*], we do not have the necessary surface roughness measurements needed for estimating  $N$  as normal stress and slip rate are varied in our experiments.

A flexible empirical relation that produces good fits to the observations is

$$k = k_0 + \beta A^n. \tag{7}$$

The motivation for the power law dependence on fractional area comes from (6b). The inclusion of a nonzero intercept  $k_0$  is physically unrealistic, as the stiffness should go to zero at zero contact area. However, the intercept is necessary because the narrow range of fractional area sampled in the experiments is insufficient for extrapolation to near-zero contact area. Fortunately, the range is narrow enough that the data at fixed normal stress are linear (Figure 7). Equation (7) can accommodate our observations and more general applications, perhaps, such as when contact area is an order of magnitude or more higher than in our experiments [*Dieterich and Kilgore, 1994, 1996*], where significant wear product is produced during sliding on initially bare surfaces [*Beeler et al., 1996*] and for simulated gouge layers [*Marone et al., 1990*], cases where the relation between fault normal stiffness and fractional contact area may be quite different than observed in our specific calibration experiments. Equation (7) with  $n = 1$  well predicts the relations between stiffness and fractional contact area at constant normal stress (Figure 7). The fit values of  $k_0$  and  $\beta$  at each normal stress are listed in Table 2.

#### 4.2.2. Application to Nontransparent Samples and to Transient Behavior

Without an adequate mechanical model to relate contact area and stiffness, we cannot determine the calibration between these quantities for use with nontransparent samples where contact area is unknown. In lieu of a quantitative model, in principal, percent changes in contact area might be inferred from percent changes in stiffness using friction theory [*Nakatani, 2001; Nagata et al., 2012*]. Unfortunately, our observations are not of sufficient quality to do so reproducibly. However, we are able to show empirically that the proportionality between changes in contact area and stiffness at fixed normal stress, equation (7), extends to some nonsteady state conditions. For an example consider a single order of magnitude change in slip rate that has large excursions of fault strength and contact area from their steady state values (Figure 8).

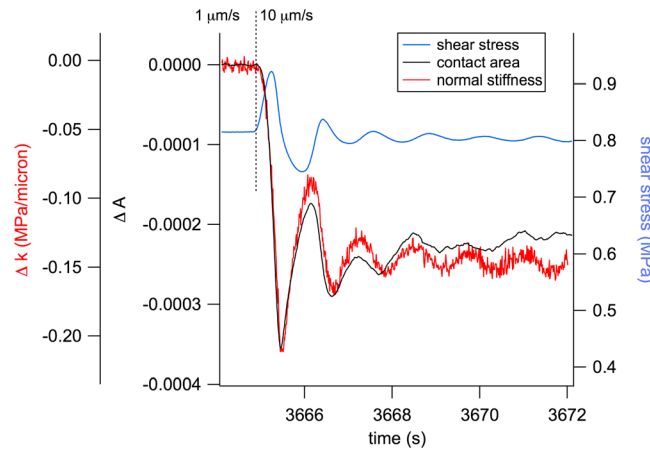


**Figure 8.** Change in contact area (black, left axis) measured in a velocity step test, from 1 to 10  $\mu\text{m/s}$ . Also, shown are changes in fault normal stiffness (red, leftmost axis), from acoustic transmission data, and for reference the shear stress (blue, right axis) during the test.

Some of the sliding rate step increases are nearly unstable, producing relatively large variations in friction between the starting and eventual steady state values. The measured fractional changes in contact area show some displacement or time-dependent drift, whereas the friction and stiffness do not. Reproducibility of contact area between identical tests is generally lower than for acoustic transmission. Stacking the data can remove much of the drift. Regardless, in this particular example, which is typical, even without attempting to reduce the variability in the direct contact area measurements, changes in stiffness are very similar to the changes in contact area. To further illustrate this idea, another case where contact area and stiffness are linear is

during a hold test [Dieterich, 1972] (Figure 9). In the test the fault is sliding at a steady state velocity when loading velocity is set to zero at time equal to zero in Figure 9; the fault continues to slip under the shear load, and as the fault slips, the measured shear stress (blue) relaxes. Accompanying the stress decrease are increases in contact area (black) and fault normal stiffness (red). The data shown are from 3, 300 s hold tests that have been stacked. The change in stiffness relative to the starting value is exactly proportional to the change in contact area. These observations from hold tests are reproducible and support the previously made hypothesis [Nagata et al., 2008, 2012] from theory [Nakatani, 2001] that changes in contact area and fault stiffness are proportional. There are, however, significant limitations as we showed in our earlier qualitative discussion of normal stress changes (Figures 3 and 7). Furthermore, during the reload following hold tests, contact area and stiffness do not closely track one another. The origin of these differences is beyond the scope of the present study.

**4.2.3. Future Laboratory Work**

A significant improvement to the present study would be to better characterize the contact size distribution using more detailed optical observations. Our light intensity measurements produce no information on the

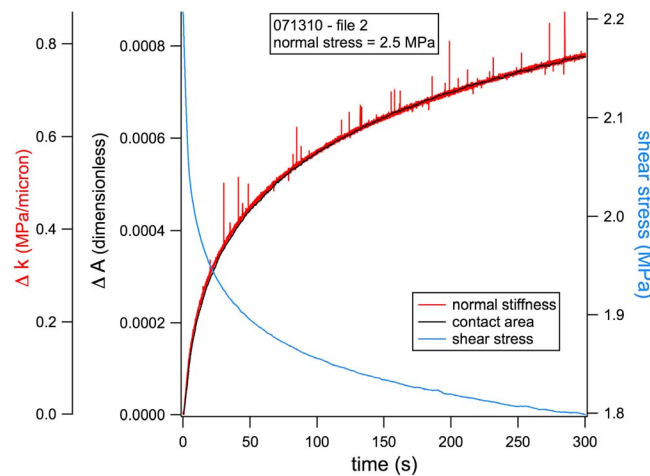


**Figure 9.** Change in contact area (black, left axis) measured in 3, 300 s hold tests, stacked to produce the average response. The initial value of the fractional contact area is 0.00245 and the final value of contact area expressed as a percent change from the initial values is 32%. Also, shown are the changes in fault normal stiffness (red, leftmost axis) and, for reference, the shear stress (blue, right axis) during the stress relaxation.

distribution of contact sizes nor on how those distributions change with slip speed and normal stress. In addition to using light intensity Dieterich and Kilgore [1994, 1996] used digital imaging to determine average contact size and the distribution of sizes. Employing this more detailed optical approach would allow us to resolve whether there are changes in average contact size and track their distribution. Related to average contact size is the characteristic contact radius or slip weakening distance  $d_c$  which is measured in rate stepping tests. The assumption of friction theory is that  $d_c$  is constant, independent of normal stress and slip velocity, an effective restatement of Greenwood and Williamson's analysis, and there is experimental evidence to support this in prior studies of bare rock surfaces [Beeler et al., 1996; Goldsby and Tullis, unpublished, 2014]. Some

confirmation of this can be made simply by determining the apparent slip weakening distance from inverting rate stepping data [Reinen and Weeks, 1993] over the entire range of normal stresses and slip speeds [Mair and Marone, 1999]. Similarly, changes in normal stress produce transients with apparent characteristic slips; these distances can be rigorously determined and compared with those from rate step tests and with average contact radius determined from imaging. Finally, to address the effects of changing slip speed and normal stress on contact area and stiffness, a combination of surface profiling and more sophisticated statistical models of rough surfaces in contact [Greenwood and Williamson, 1966; Brown and Scholz, 1983; Yoshioka, 1994] should be further investigated.

While such approaches should produce a clearer understanding of the relationship between contact area and fault stiffness, the cases of interest to natural fault mechanics are for rocks at higher normal stresses, at elevated temperature in reactive fluids, and possibly in the presence of significant fault gouge. Whether or not the empirical calibration of acoustic transmission data can be applied to infer contact area under such conditions may be of greater practical need than a deeper understanding of the contact-scale micromechanics of room temperature friction in the laboratory. To that end, work on bare granite [Nagata *et al.*, 2012] and fault gouge [Nagata, 2008] qualitatively indicate that AT can be broadly applied at room temperature to infer fractional changes in contact area.

## 5. Implications for Postseismic Changes in Natural Fault Zones

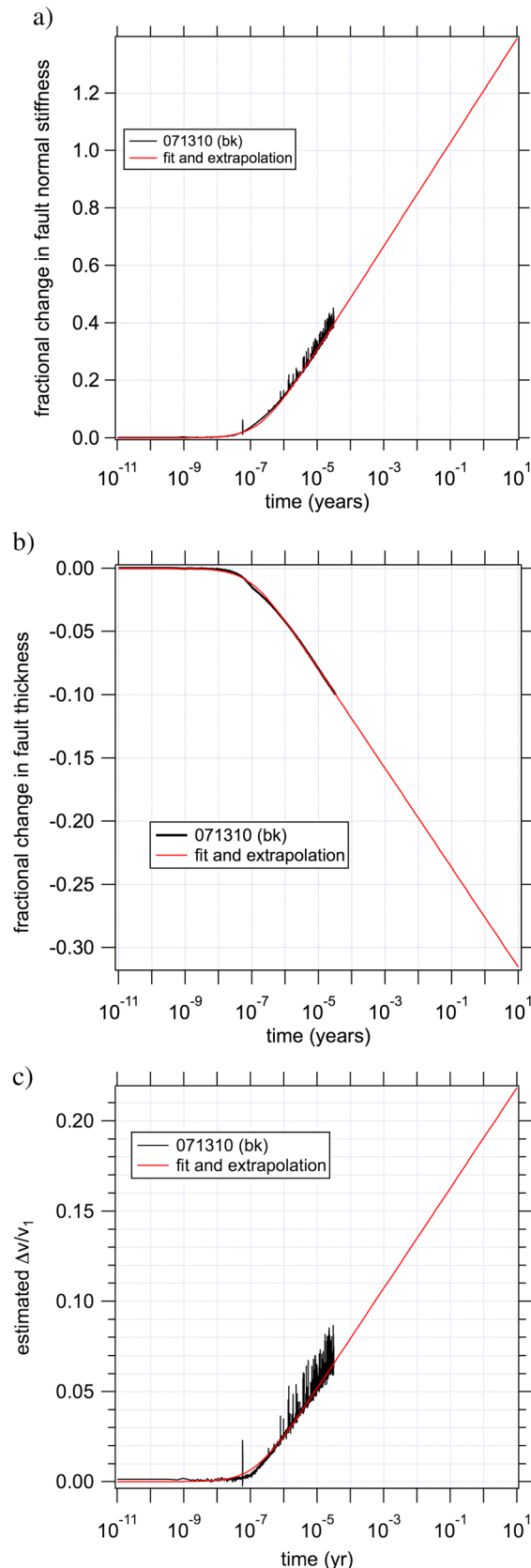
The changes in contact area and fault stiffness observed in our experiments can be relatively large. For example, during a 300 s hold test, contact area increases by ~30% over the steady state value (Figure 9). If the processes responsible were operating in a natural setting, whether such changes within a narrow fault zone could be detected depends on how the change in contact area is manifested in elastic properties, on the frequency of the incident waves, on the path length of incident waves, and on the spatial scale over which the change occurs. To determine the implications of our observations for natural fault properties, in the following sections we consider the dimension of natural fault zones relative to our very idealized experiments, the implied changes in elastic properties from our experiments, and the wave frequencies used to detect changes in fault properties in natural settings.

The prevailing structural description of natural, large displacement, strike-slip fault zones comes from observations at the Punch Bowl and North San Gabriel faults of the San Andreas system in southern California [Chester and Logan, 1986; Chester *et al.*, 1993; Chester and Chester, 1998]. For these two segments that have undergone tens of km of slip, the fault zone can be divided into a fault core and a damage zone based on the intensity of inelastic deformation relative to the background level within the host rock. Virtually, all the fault offset occurs in the core; it is intensely deformed, consisting of cataclases, ultracataclases, highly comminuted fault gouge, and altered materials. The damage zone accommodates almost no shear strain relative to the core though it is nonetheless fractured, faulted, and altered. The damage zone and fault core have half-lengths on the order of a few hundreds of meters and decimeters to meters, respectively.

Time-dependent postseismic increases in wave speed within the damage zone following major strike-slip earthquakes [e.g., Li *et al.*, 1998, 2006; Li and Vidale, 2001] have been attributed to the closure of dilatant cracks using elastic models of cracked solids with distributed, randomly oriented dilatancy [Garbin and Knopoff, 1975; O'Connell and Budiansky, 1974]. Wave speeds from fault zone guided waves induced by active sources are consistent with the idea that the damage zone is more compliant, the wave speed being 30 to 50% smaller in the damage zone than in the surrounding rock [Li *et al.*, 1998; Li and Vidale, 2001]. While such isotropic crack dilatancy might be generated within the damage zone by stress concentrations at the tip of a propagating rupture [Andrews, 2005], damage should be more concentrated in the decimeter- to meter-scale fault core because stress and strain associated with fault slip and rupture propagation increase with proximity to the fault surface [Chester *et al.*, 2004] and because frictional slip is highly dilatant. Thus, the core is both the region of greatest mechanical interest in measuring postseismic changes in properties and may be the most highly dilated and damaged region within the broader fault zone.

### 5.1. Implied Changes in Wave Speed

Acknowledging the differences between our experiments and crustal faults at shallow depths in material (Lucite), temperature (25°C), and normal stress (2.5 MPa), we take the laboratory fault to be an example end-member case of a highly localized fault core and estimate changes in fault properties from our measurements



for comparison with field observations. Naturally, observed changes in wave speed are interpreted in the context of the seismic velocity of models of a cracked solid [e.g., *O'Connell and Budiansky, 1974*]. These models are derived for static loading conditions but are applied to dynamic wave propagation. The derived velocities therefore are assumed to be frequency independent. While the same frequency independence may not apply to thin tabular fault zones, for the purpose of qualitative comparison, in the immediately following analysis we put our measurements of transmitted amplitude into the same static and frequency-independent context by estimating an effective wave speed of the fault zone. This analysis is an attempt to determine whether the lab-observed changes are of a similar magnitude to those observed in nature. The analysis relies on the theory that the specific stiffness  $k$  in equation (3) is identical for static and dynamic conditions and therefore is a frequency-independent elastic property [*Pyrak-Nolte et al., 1990*]. While measurements show static and dynamic stiffness differ somewhat [*Pyrak-Nolte et al., 1990*], they are of the same order. The differences are thought to be due to inelastic effects not accounted for in elastic wave speed estimates and therefore not relevant to the following simple calculation.

**Figure 10.** Changes in fault zone properties with time. (a) Measured fractional changes in fault stiffness (black) collected during three stacked 1000 s hold tests. A fit of the data using the same form as equation (9) is shown also (red) that could be used for extrapolation. The fit values are  $t_c = 2 \times 10^{-7}$  years and the coefficient to the logarithmic term is 0.078. Equivalently, the coefficient is 0.18 for a fit to the data using  $\log_{10} t$  (18% change per decade). (b) Measured fractional changes in fault thickness (fault normal strain) from normal displacement data (black) collected during three stacked 1000 s hold tests. A fit of the data using the same form as equation (9) is shown also (red) that is used to extrapolate for comparison with postseismic geodetic data. The fit values are  $t_c = 9.5 \times 10^{-8}$  years and the coefficient to the logarithmic term is  $-0.017$ . Equivalently, the coefficient is  $-0.04$  for a fit to the data using  $\log_{10} t$  (4% change per decade). (c) Implied fractional changes in wave speed calculated from dynamic fault stiffness and normal displacement data (black) collected during three stacked 1000 s hold tests. A fit of the data using equation (9) is shown also (red). The fit values are  $t_c = 1.4 \times 10^{-7}$  years and the coefficient to the logarithmic term is 0.012. Equivalently, the coefficient is 0.03 for a fit to the data using  $\log_{10} t$  (3% change per decade).

Wave speeds are calculated from the experimentally measured specific stiffness and fault normal displacement during hold tests, and the natural data are from postseismic active source seismic measurements. Slip and strength during a hold test is similar to post seismic slip in that the fault undergoes no active loading and slip speed decays gradually over time. Fault strength is thought to increase in both situations—this is despite, in the case of the laboratory fault, the shear stress decreasing as the fault continues to slip, and, in the case of natural faults there being no measurements of postseismic stress or strength. In the present study, the laboratory data used are a stack of 3, 1000 s holds. Normal displacement measurements are converted to fault thickness by assuming the fault is approximately 4 times the RMS roughness of the fault surfaces. The roughness is 6.1  $\mu\text{m}$ , resulting in an estimated thickness of approximately 24  $\mu\text{m}$ , assumed to be the steady state thickness at 1  $\mu\text{m/s}$  slip rate. Knowing the fault thickness and stiffness allows an estimate of the wave speed,  $v = \sqrt{M/\rho}$ , where  $M$  is the elastic modulus and  $\rho$  is the solid density of the fault zone. The specific stiffness is  $k = M/w$ , where  $w$  is the fault zone thickness. The fault zone solid density is  $\rho = m/A_T w$  where  $m$  is solid mass. Therefore, the wave speed relates to specific stiffness and fault zone thickness as  $v = w\sqrt{kA_T/m}$ . Fractional changes in wave speed are

$$\frac{\Delta v}{v_1} = \frac{w\sqrt{k}}{w_1\sqrt{k_1}} - 1, \quad (8)$$

where the subscript 1 indicates the initial or reference value from which the change is measured. During a hold test the fault zone thickness decreases (Figure 10b), presumably due to fault normal deformation at asperity contacts [e.g., *Dieterich*, 1972]. Simultaneously, the specific stiffness increases (Figure 10a), also presumably because of inelastic, fault normal deformation that increases the contact area and stiffness of individual asperity contacts. The net effect estimated using (8) is an increase in the implied wave speed with time (Figure 10c) that follows a well-defined logarithmic trend that can be fit with the empirical relationship

$$\frac{\Delta v}{v_1} = v_r \ln\left(\frac{t}{t_c} + 1\right). \quad (9)$$

The resulting fraction rate of wavespeed change per natural logarithm of time is  $v_r = 0.012$  and the cutoff time  $t_c = 1.4 \times 10^{-7}$  years. The extrapolation to between 1 and 10 years (Figure 10c) shows net fractional changes of 19 and 22%, respectively. In comparison to changes observed in active source studies, the extrapolated changes in fault core wave speeds between specific years are smaller: changes of 0.8% between 2 and 4 years, 0.5% between years 4 and 6 and 0.3% between years 6 and 8. Thus, the implied wave speed changes are at least 2 times smaller than observed at Landers for comparable time periods for  $S$  and  $P$  waves [*Li et al.*, 1998; *Li and Vidale*, 2001] and are not consistent with the naive expectation that the fault core will undergo larger recovery than the damage zone.

## 5.2. Fault Zone Thickness Changes

Comparison can also be made between natural postseismic and laboratory fault normal contraction. Like the changes in stiffness and contact area, the fault normal displacements are a large fraction of the total thickness of the fault zone, 0.1 in 1000 s (Figure 10b). Thickness changes during a stress relaxation test on bare rock surfaces follow the same form as equation (9) [*Beeler and Tullis*, 1997], a result that in hindsight is implied by *Dieterich* [1972]. Similar but not identical thickness changes are found for simulated gouges [*Beeler and Tullis*, 1997; *Marone*, 1998]. A fit to the Lucite data yield a fractional rate of contraction per natural logarithm of time of 0.017 and a cutoff time  $t_c = 9.5 \times 10^{-8}$  years. An extrapolation to 3.3 years for comparison to fault normal displacement measured by *Savage et al.* [1994] following the 1989 Loma Prieta earthquake results in fractional normal displacement (fault normal strain) of 0.3. *Savage et al.* [1994] estimate 0.1 m of fault normal displacement. If similar processes were operating in both the lab and nature, resulting in equivalent strains, the Loma Prieta fault normal contraction could be accommodated within a shear zone of 0.34 m thickness. In other words, the GPS and lab observations of fault normal contraction can be reconciled with field deformation within the thin decimeters scale fault core as defined by the studies of exhumed faults [*Chester et al.*, 2004], rather than in the broader damage zone.

## 5.3. Detecting Changes in Shear Zone Properties

The displacement discontinuity method used to derive equation (3), is appropriate for seismic characterization of features such as cracks and faults that are longer than the wavelength measured perpendicular to the wave

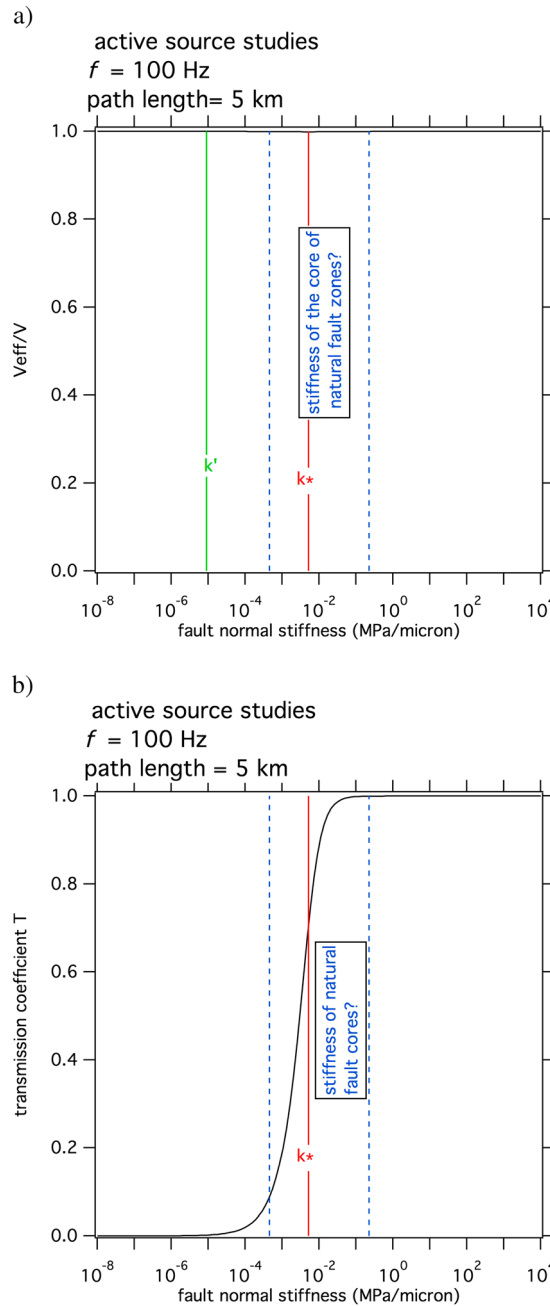


**Figure 11.** Estimates relevant to the detection of changes in elastic properties of natural fault cores using the displacement discontinuity solution of Pyrak-Nolte et al. [1987]. (a) Effective wave speed  $v_{\text{eff}}$ , the combined wave speed of the surrounding rock, and a fault core, normalized by the wave speed of the surrounding rock,  $v_p$ , calculated from equation (10) as function of the fault normal stiffness of the fault core. Here the path length  $L = 5 \text{ km}$ ,  $v_p = 5.5 \text{ km/s}$ ,  $\rho = 3 \text{ g/cm}^3$ , and  $f = 100 \text{ Hz}$ . The implied values of  $k_* = 0.0052 \text{ MPa}/\mu\text{m}$  and  $k_* = 9 \times 10^{-6} \text{ MPa}/\mu\text{m}$  are shown. Also, shown for reference are estimates of the upper and lower bounds of the stiffness of the core of natural faults (blue-dashed lines) assuming the core width ranges from 0.2 to 2 m and a  $P$  wave modulus between 0.5 M and 0.01 M with  $M = 90 \text{ GPa}$ . (b) The transmission coefficient with stiffness from equation (3) using the same material values and wave speed as in Figure 11a.

path but much thinner than the wavelength normal to the path. In our experiments the fault is  $\sim 16 \text{ mm}$  long and  $\sim 24 \mu\text{m}$  thick, while wavelength is  $\sim 2.5 \text{ mm}$ . The method also may be appropriate for extrapolation to the core of natural fault zones thought to be meters to decimeters in thickness with lateral extension of many tens to hundreds of kilometers. To determine whether active seismic sources having frequencies and wavelengths in the range of 100 Hz and 50 m, respectively, may be able to image the slipping portion of active faults, in this section we apply the displacement discontinuity equation to formally consider the expected travel times and the transmission coefficients of the core shear zones of natural faults.

Active source methods used in studies of postseismic fault properties characterize the average wave speed along the path, inferred from travel time. Taking the combined, “effective”, wave speed  $v_{\text{eff}}$  to be that of the fault zone and the surroundings, and  $v_p$  as the wave speed of the surroundings, their ratio is

$$\frac{v_{\text{eff}}}{v_p} = \frac{1 + \left(\frac{k_*}{k}\right)^2}{1 + \left(\frac{k_*}{k}\right)^2 + \frac{k'}{k}} \quad (10)$$

[Pyrak-Nolte et al., 1987], where  $k' = v_p^2 \rho / L$  and  $L$  is the path length from the source to the receiver.  $k'$  is the stiffness of the surrounding region along the wave path (Figure 11a).

Shown for reference in Figure 11a are estimates of the possible maximum and minimum stiffness of the core of natural fault zones. These estimates assume that the range of fault width is 2 to 0.2 m, consistent with the evidence from exhumed faults [Chester et al., 2004] and the fault  $P$  wave modulus is between 0.5 M and 0.01 M. The upper bound on the modulus, 0.5 M, comes from assuming the fault core cannot have a modulus that exceeds that of the surrounding damage zone, using data from the static deformation of natural faults [Fialko et al., 2002], 0.43 to 0.6 M. Although this estimate is for the shear modulus, we take it to be a reasonable bound. The lower bound is from our experiments. The modulus of Lucite plastic is  $M = 7.9 \text{ GPa}$ . At the beginning of the hold the normal stiffness is  $2.5 \text{ MPa}/\mu\text{m}$ . For the estimated fault thickness,  $24 \mu\text{m}$ , the fault modulus is 60 MPa, on the order of 0.01 M.

In the extrapolated calculations  $M$  is 90 GPa, consistent with undamaged rock. The wave speed ratio (10) is  $\sim 1$  for all core stiffnesses in

this range, and indeed for the entire range considered. If the same processes that change fault properties within the slipped zone in the laboratory experiments were operating in the field, we conclude that seismic imaging studies using travel time would not detect the changes.

This invisibility may not extend to active source studies if transmitted amplitude is measured instead of travel time. Figure 11b shows the transmission coefficient calculated using equation (3) for the same conditions. The estimated range of natural fault core stiffnesses coincides with the range where the transmission coefficient varies strongly with specific stiffness,  $dT/dk > 0$ , where changes in stiffness may be detectable. Furthermore, the implied postseismic time-dependent changes in fault stiffness from our experiments are quite a bit larger than for the implied wave speed, exceeding 100% in 0.1 years (Figure 10a). The per decade change in fault stiffness is 18% and, for example, if measured between postseismic years 2 and 4, the expected changes are 5%. The prediction from this extrapolation in scale and frequency is preliminary, is based on a simplified discontinuity model, assumes high contrast between the fault and the surrounding material, and should be verified and compared with more sophisticated models such as those where the fault core has a finite thickness and in which the surroundings are also damaged and recovering.

## 6. Summary

In friction tests on a transparent rock analogue material, Lucite, transmitted light and high-frequency active seismic imaging techniques were employed simultaneously to determine contact area and specific fault normal stiffness. Contact area and stiffness covary at all conditions tested. The variation is not unique; instead of a single calibration curve, the scaling of fault stiffness with contact area depends on slip speed and on normal stress. It is not possible to infer absolute contact area from measurements of fault stiffness without further advances in theory and modeling of contacting rough surfaces. However, with some limitations, at constant normal stress under specific conditions it is possible to equate changes in fault stiffness to changes in contact area. Changes in contact area are proportional to changes in fault normal stiffness during rate stepping and hold tests which may allow monitoring of contact area increases during laboratory tests that measure interseismic strength recovery. We are optimistic that this approach will produce deeper knowledge of the contact-scale processes that underlie rock friction and that control earthquake occurrence times and nucleation. However, for example, during changes in normal stress and during reloading following hold tests contact area and stiffness do not closely track one another.

To make comparisons between the lab and field-measured changes in fault zone properties such as postseismic increases in wave speed or fault normal strain following large earthquakes, it is the fault normal stiffness and normal displacement, rather than the contact area, that are the comparable quantities. Fault zone normal stiffness, thickness, and the implied wave speed follow a logarithmic dependence on time during stress relaxation tests. These changes imply postseismic wave speed changes on the order of 0.3% to 0.8% per year in the few years following an earthquake, smaller by a factor of about 2 than natural increases seen following the 1992 Landers earthquake and elsewhere. Formal analysis of detectability suggests that changes in the core shear zones of natural faults will be invisible to waves with frequencies on the order of 100 Hz using travel time. The postseismic changes in stiffness are much larger and should be visible in the field using changes in reflection/transmission coefficient. Lab-measured fault normal strains during relaxation tests are tens of percent. If the natural observed fault normal displacements ( $\sim 0.1$  m) represent equivalent strains to those seen in our experiments, the fault normal deformation occurs within narrow, decimeter scale fault zone. These encouraging results notwithstanding, there are numerous, significant differences between these laboratory tests and postseismic field observations that need further consideration. In particular, our faults are in an analogue material, the normal stresses are small relative to overburden in the seismogenic zone, and the hold tests used are not an exact analogue for the immediate postseismic period.

## Appendix A: Data and Data Corrections

The direct shear geometry (Figures 1 and 2) has a continuous displacement limit that depends on the sample dimension. Frictional properties of a newly prepared bare rock surface or gouge layer are displacement dependent over many millimeters or more of slip [e.g., *Dieterich, 1981*], which complicates measuring fault properties reproducibly. To overcome the displacement limitation, the fault is often slid and reset a number

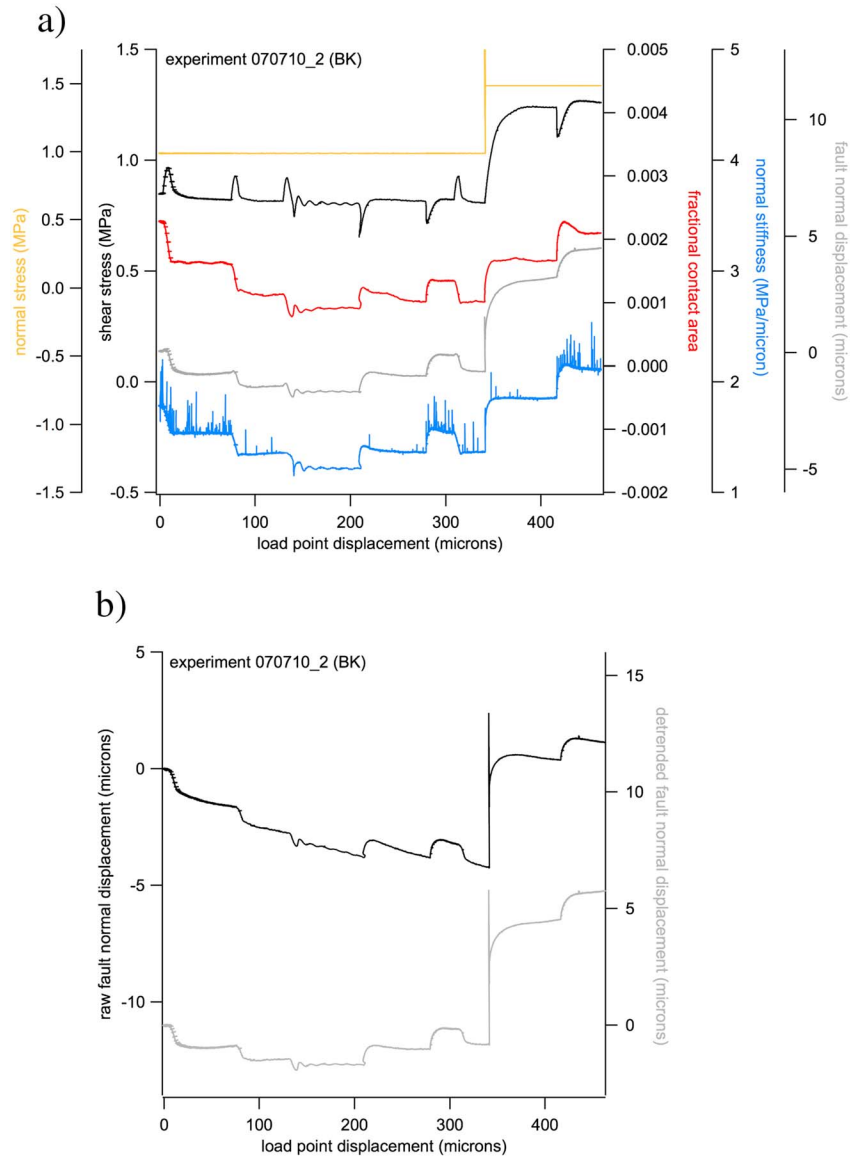


**Figure A1.** (a) Experiment showing shear stress, normal stress, contact area, fault normal stiffness, and fault normal displacement versus the load point displacement of the servo control system. The sequence consists of sliding initially at 1  $\mu\text{m/s}$  and 1 MPa normal stress, two subsequent order of magnitude step decreases in loading velocity, three order of magnitude steps up in velocity and then an order of magnitude step down. Subsequent to that is a step up in normal stress (at around 350  $\mu\text{m}$  displacement) to 1.5 MPa, followed by an order of magnitude step down in loading velocity. All of the measurements shown are the scaled raw data except the fault normal displacement that has been corrected for a linear trend and for elastic deformation in the material surrounding the fault associated with the step change in normal stress. (b) Correction of the linear trend in the fault normal displacement. The raw data are shown in black and the detrended data are in grey. The grey trace in Figure A1a is the detrended data shown here in Figure A1b corrected for elastic effects using equation (A1).

of times until shear resistance, and other fault properties are slip independent. This is less of a problem for Lucite and typically only a millimeter or so of slip is required to reach displacement independent friction. Figure A1 shows scaled raw shear stress, normal stress, contact area, transmitted amplitude, and fault normal displacement during an experiment containing a sequence of rate steps and a single normal stress step. With the exception of fault normal displacement, there are no significant displacement dependencies and none of the data in this study have been corrected for displacement. The exception, the fault normal displacement data, has a linear displacement-dependent trend that results likely from wear of the fault surface or from misalignment of the sensor. Figure A1b shows the raw fault normal displacement and the same measurements corrected by removing a linear slip-dependent trend.

There are two additional necessary machine corrections to the normal displacement data when the normal stress is changed. The transducer that measures normal displacement and its target on the other side of the fault are each mounted some distance away from the fault in the fault normal direction. So the normal displacement measures elastic distortion within the bulk as well as across the interface. For a change in normal stress there is strain in the bulk of the same sense as the strain across the interface; that is, for an increase in normal stress there is compressive strain in the bulk and across the interface. The extraneous strain can be removed by approximating it by that resulting from a uniaxial stress change, a change in the loading stress labeled  $\sigma_n$  in Figure 1. In addition, in the direct shear geometry an increase in average shear stress at the interface is accompanied by an increase in thickness of the fault blocks as measured normal to the interface. This correction can be approximated by the strain resulting from the Poisson effect of changing the loading stress labeled  $\tau$  in Figure 1. The combined correction to the measured normal displacement  $\delta_n$  is

$$\delta_n^{cor} = \delta_n - L \left[ \frac{(\sigma_e - \sigma_0)}{E} - \frac{\nu(\tau - \tau_0)}{E} \right], \quad (A1)$$

where  $L$  is the distance between the mounting points of transducer and target (11 mm),  $E$  is Young's modulus (3 GPa),  $\nu$  is Poisson's ratio (0.32), and  $\sigma_0$  and  $\tau_0$  are arbitrarily chosen reference values of normal and shear stress. In the example shown in Figure A1 the reference values are those associated with sliding at a slip speed of 1  $\mu\text{m/s}$  at 1 MPa normal stress (1 MPa, 0.82 MPa), respectively. The data shown in Figure 3b have also been corrected using (A1). In that case the references are 0.5 MPa and 0.42 MPa, respectively. The corrected normal displacement measurement may be qualitatively useful in understanding transmitted amplitude because the derivative of normal stress with respect to normal displacement is the static normal stiffness of the fault and thus should scale similarly to the specific normal stiffness that appears in equation (3) (see section 5).

#### Acknowledgments

Funding for acoustic transmission instrumentation and data acquisition, and for Kohei Nagata's travel and expenses were paid by a joint grant from the USGS Venture Capital Fund to the USGS Earthquake Science Center and the Earthquake Research Institute. Additional support for research related to acoustic transmission and normal stress changes was provided by a grant from the Southern California Earthquake Center. SCEC is supported by NSF cooperative agreement EAR-0106924 and USGS cooperative agreement 02HQAG0008. This is SCEC contribution 1952. This study was also supported by the Ministry of Education, Culture, Sports, Science, and Technology (MEXT) of Japan under its Earthquake and Volcano Hazards Observation and Research Program. This report was significantly improved in response to JGR reviews by Chris Marone and Brett Carpenter, to USGS internal reviews by Carolyn Morrow and Ole Kaven, and to reviews of an earlier version of the manuscript by Joerg Renner, Mandy Duda, and an anonymous referee. The data in this paper are available from the corresponding author.

#### References

- Andrews, D. J. (2005), Rupture dynamics with energy loss outside the slip zone, *J. Geophys. Res.*, *110*, B01307, doi:10.1029/2004JB003191.
- Beeler, N. M. (2007), Laboratory-observed faulting in intrinsically and apparently weak materials: Strength, seismic coupling, dilatancy, and pore fluid pressure, in *The Seismogenic Zone of Subduction Thrust Faults*, edited by T. Dixon and C. Moore, Columbia Univ. Press, New York.
- Beeler, N. M., and S. H. Hickman (2001), A note on contact stress and closure in rock joint and fault models, *Geophys. Res. Lett.*, *28*, 607–610, doi:10.1029/2000GL014548.
- Beeler, N. M., and T. E. Tullis (1997), The roles of displacement in velocity dependent volumetric strain of fault zones, *J. Geophys. Res.*, *102*, 22,595–22,609, doi:10.1029/97JB01828.
- Beeler, N. M., T. E. Tullis, M. L. Blanpied, and J. D. Weeks (1996), Frictional behavior of large displacement experimental faults, *J. Geophys. Res.*, *101*, 8697–8715, doi:10.1029/96JB00411.
- Beeler, N. M., T. E. Tullis, and D. L. Goldsby (2008), Constitutive relationships and physical basis of fault strength due to flash-heating, *J. Geophys. Res.*, *113*, B01401, doi:10.1029/2007JB00498.
- Bowden, F. P., and D. Tabor (1950), *The Friction and Lubrication of Solids*, 374 pp., Oxford Univ. Press, New York.
- Brown, S. R., and C. H. Scholz (1985), The closure of random elastic surfaces in contact, *J. Geophys. Res.*, *90*, 5531–5545, doi:10.1029/JB090iB07p05531.
- Byerlee, J. D. (1978), Friction of rocks, *Pure Appl. Geophys.*, *116*, 615–626.
- Chester, F. M., and J. S. Chester (1998), Ultracataclastic structure and friction processes of the San Andreas fault, *Tectonophysics*, *295*, 199–221.
- Chester, F. M., and J. M. Logan (1986), Implications for mechanical properties of brittle faults from observations of the Punchbowl fault zone, California, *Pure Appl. Geophys.*, *124*, 79–106.
- Chester, F. M., J. P. Evans, and R. L. Biegel (1993), Internal structure and weakening mechanisms of the San Andreas fault, *J. Geophys. Res.*, *98*, 771–786, doi:10.1029/92JB01866.
- Chester, F. M., J. S. Chester, D. L. Kirschner, S. E. Schultz, and J. P. Evans (2004), Structure of large-displacement, strike-slip fault zones in the brittle continental crust, in *Rheology and Deformation in the Lithosphere at Continental Margins*, edited by G. D. Karner et al., pp. 223–260, Columbia Univ. Press, New York.
- Dieterich, J. H. (1972), Time-dependent friction in rocks, *J. Geophys. Res.*, *77*, 3690–3697, doi:10.1029/JB077i020p03690.
- Dieterich, J. H. (1978), Time-dependent friction and the mechanics of stick slip, *Pure Appl. Geophys.*, *116*, 790–806.
- Dieterich, J. H. (1979), Modeling of rock friction: 1. Experimental results and constitutive equations, *J. Geophys. Res.*, *84*, 2161–2168, doi:10.1029/JB084iB05p02161.
- Dieterich, J. H. (1981), Constitutive properties of faults with simulated gouge, in *Mechanical Behavior of Crustal Rocks*, Geophysical Monograph, vol. 24, edited by N. L. Carter et al., pp. 103–120, AGU, Washington, D. C.
- Dieterich, J. H., and B. D. Kilgore (1994), Direct observation of frictional contacts: New insights for state-dependent properties, *Pure Appl. Geophys.*, *143*, 283–302.
- Dieterich, J. H., and B. D. Kilgore (1996), Imaging surface contacts: Power law contact distributions and contact stresses in quartz, calcite, glass and acrylic plastic, *Tectonophysics*, *256*, 219–239.
- Fialko, Y., D. Sandwell, D. Agnew, M. Simons, P. Shearer, and B. Minster (2002), Deformation of nearby faults induced by the 1999 Hector Mine earthquake, *Science*, *297*, 1858–1862.
- Garbin, H. D., and L. Knopoff (1975), Elastic moduli of a medium with liquid-filled cracks, *Quart. Appl. Math.*, *33*, 301–303.
- Goodman, R. E. (1976), *Methods of Geological Engineering in Discontinuous Rocks*, 472 pp., West, New York.

